Superradiant absorption in multiple optical nanoresonators

Soongyu Yi, Ming Zhou, Zhu Wang, and Zongfu Yu*

Department of Electrical and Computer Engineering, University of Wisconsin, Madison, Wisconsin 53706, USA

(Received 10 February 2014; revised manuscript received 23 April 2014; published 30 May 2014)

Optical resonators offer an excellent analog of quantum two-level systems. Studying optical analogs of the electromagnetically induced transparency and the Fano interference has greatly stimulated the field of nanophotonics. In this context, the theoretical analysis is developed for the optical analog of superradiance in multiple nanoresonators. Unique superradiant effects are found for light absorption in nanoresonators, such as superradiance-induced transparency.

DOI: 10.1103/PhysRevB.89.195449 PACS number(s): 42.82.Et, 42.25.−p, 78.67.Pt, 78.67.Wj

Discovered by Dicke in 1954 [1], superradiance describes a collective coherent effect in a cluster of identical quantum emitters: A single quantum emitter prepared in the upper level creates spontaneous emission with an intensity I; when N emitters are placed together within a wavelength dimension, the total emission intensity grows to N^2I, instead of the incoherent addition NI. The emitters have no direct near-field coupling, and yet their phases are synchronized. Such in-phase oscillation is mediated through the free-space field that they radiate to.

Compared to the analogs [2–11] of electromagnetically induced transparency (EIT) [12] and Fano [13] interference, the optical analog of superradiance is more challenging to achieve. It requires N nanoresonators with deep subwavelength sizes placed within a wavelength dimension [14]. While the superradiance can be created with properly managed near-field interactions, which will be discussed later, a faithful analog of quantum emitters requires the near-field interaction to be minimal. The requirements of subwavelength sizes [15] and minimal near-field interaction rule out many nanoresonator candidates. In addition to the challenges in the implementation, theoretical treatments developed for quantum emitters also need to be adapted to include the light absorption in nanoresonators, which is of practical importance for optoelectronic devices.

In this paper, we developed a classical optical theory for the analog of superradiance based on a multiresonator multichannel temporal coupled mode theory. The theory reveals unique superradiant absorption effects, such as superradiance-induced transparency where total absorption of N resonators is suppressed by a factor of $1/N$. This suppression effect is in great contrast to the enhancement effect in superradiant emission. It is also in great contrast to an intuitive dipole-approximation picture that is used to explain the N^2 emission enhancement [16]. The dipole approximation would predict that the absorption increases linearly with N. To validate theoretical predictions, we simulate the analog of superradiance using graphene ribbon resonators [17–20], which offer deep subwavelength sizes as well as easy control of near-field interactions.

We note that the superradiant effect has been frequently noted in two-resonator systems in the optical analogs of EIT and Fano interferences [2,21–23]. In addition, the N resonator has also been studied before, but it was treated in an incoherent manner without considering either the near-field or the far-field interactions among resonators [24,25]. The work here provides a complete theoretical treatment of the N-resonator system and demonstrates unique superradiant absorption effects.

We start by considering a cluster of N optical resonators. The damping mechanism in the resonator includes the light absorption by materials and the coupling to the free-space radiation. The dynamics can be described by a temporal coupled mode theory [26,27]. From energy conservation and time-reversal symmetry, one can obtain the equation governing the interaction between multiple resonators and multiple free-space radiation channels [21,28]:

$$\frac{d}{dt}\boldsymbol{a} = (i\Omega - \Gamma)\boldsymbol{a} + D^T \boldsymbol{S}_{\text{in}}, \tag{1}$$

where $\boldsymbol{a} = (a_1, a_2, \ldots, a_N)$ are the amplitudes of resonators normalized such that $|a_i|^2$ is the energy stored in the ith resonator. $\boldsymbol{S}_{\text{in}} = (S_1, S_2, \ldots, S_m)$ are the amplitudes of the power flux carried by each orthogonal radiation channel. D is the coupling rate between N resonators and m free-space channels. T is the transpose operator. The Hamiltonian Ω is given by

$$\Omega = \begin{pmatrix} \omega_1 + \frac{i\gamma_1}{2} & \cdots & \Omega_{1N} \\ \cdots & \cdots & \cdots \\ \Omega_{N1} & \cdots & \omega_n + \frac{i\gamma_N}{2} \end{pmatrix}, \tag{2}$$

where ω_i and γ_i are the resonant frequencies and the absorption rates, respectively. The off-diagonal elements Ω_{ij} are the *near-field interaction* among resonators due to the overlap of near fields. In addition to the near field, there is also a *far-field interaction* among resonators, represented by $\Gamma = \frac{1}{2}D^T D$. The far-field interaction is a direct consequence of energy conservation. Because all resonators couple to the same radiation fields and their radiation amplitudes add up coherently, the resonators need to coordinate with each other in order to comply with the energy conservation law. This coordination is reflected by the far-field interaction term Γ, which is the key to the far-field superradiant effect.

The amplitudes of reflected lights are given by

$$\boldsymbol{S}_{\text{out}} = C\boldsymbol{S}_{\text{in}} + D\boldsymbol{a}, \tag{3}$$

where C is a $m \times m$ matrix representing the direct transmission from the incident to the outgoing channels without routing through the resonators.

*zyu54@wisc.edu

We start by considering a faithful analog of quantum emitters: N identical resonators couple to a single radiation channel. Without any near-field interaction, $\Omega = (\omega_0 + i\frac{\gamma_0}{2})\boldsymbol{I}$ is diagonal, where $\boldsymbol{I}$ is an N-dimensional identity matrix. The coupling to the channel is identical for all resonators $D = (\sqrt{\gamma_c}, \sqrt{\gamma_c}, \ldots, \sqrt{\gamma_c})$, where γ_c is the coupling rate.

First, we briefly review the superradiant emission. To study the emission, we assume no incident light $\boldsymbol{S}_{\text{in}} = 0$. For a single resonator alone, using Eqs. (2) and (3), it is easy to show that the amplitude of an excited resonator decays as $|a_i|^2 \sim \exp[-(\gamma_0 + \gamma_c)t]$. With N resonators together, the amplitude decays as $|a_i|^2 \sim \exp[-(\gamma_0 + N\gamma_c)t]$. The enhanced decaying rate due to the in-phase oscillation of all resonators directly leads to an emission intensity N times stronger for each resonator, and N^2 stronger for all resonators together.

We now focus on the superradiant absorption in the presence of an incident field $\boldsymbol{S}_{\text{in}}$. The superradiant in-phase oscillation of resonators has more complex consequences on absorption. As a reference for comparison, the absorption of a single resonator alone is

$$A_s(\omega_0) = \frac{4\gamma_0\gamma_c}{(\gamma_0 + \gamma_c)^2}. \tag{4}$$

For N resonators, we choose $C = -1$ such that D is real for Eq. (3). We take $\frac{d}{dt} = i\omega$. Equation (1) then becomes

$$a = \left[i(\omega I - \Omega) + \tfrac{1}{2}D^T D\right]^{-1} D^T \boldsymbol{S}_{\text{in}}. \tag{5}$$

Substituting Eq. (5) into Eq. (3), we have

$$\boldsymbol{S}_{\text{out}} = -\boldsymbol{S}_{\text{in}} + D\left[i(\omega I - \Omega) + \tfrac{1}{2}D^T D\right]^{-1} D^T \boldsymbol{S}_{\text{in}}. \tag{6}$$

Therefore

$$\frac{\boldsymbol{S}_{\text{out}}}{\boldsymbol{S}_{\text{in}}} = -1 + D\left[i\left(\omega - \omega_0 - i\frac{\gamma_0}{2}\right)I + \frac{1}{2}D^T D\right]^{-1} D^T. \tag{7}$$

DD^T is a scalar representing the summation of all coupling rates. Using Eq. (7), we obtain the reflection $R = \boldsymbol{S}_{\text{out}}/\boldsymbol{S}_{\text{in}}$,

$$|R(\omega)|^2 = \frac{(\omega - \omega_0)^2 + \left(\frac{\gamma_0}{2} - \frac{1}{2}DD^T\right)^2}{(\omega - \omega_0)^2 + \left(\frac{\gamma_0}{2} + \frac{1}{2}DD^T\right)^2}. \tag{8}$$

Then the absorption is

$$A_N(\omega) = 1 - |R(\omega)|^2 = \frac{\gamma_0 DD^T}{(\omega - \omega_0)^2 + \left(\frac{\gamma_0}{2} + \frac{1}{2}DD^T\right)^2} \tag{9}$$

with a peak value at the resonance frequency

$$A_N(\omega_0) = \frac{4\gamma_0 DD^T}{(\gamma_0 + DD^T)^2}, \tag{10}$$

where $DD^T = N\gamma_c$. Comparing Eqs. (4) and (10), we can see that N resonators behave as if they were just a single "macroresonator" with a coupling rate enhanced by N times. We next discuss three different regimes of superradiant absorption below.

First, for weakly absorptive resonators $\gamma_0 \ll \gamma_c$, the superradiance greatly suppresses the absorption. The absorption of a single resonator when alone is $A_s(\omega_0) \approx 4\gamma_0/\gamma_c$. Using Eq. (10), the total absorption of N resonators is

$$A_N(\omega_0) \approx \frac{1}{N}\frac{4\gamma_0}{\gamma_c} = \frac{A_s(\omega_0)}{N}. \tag{11}$$

The absorption of the individual resonator in the N-resonator system is suppressed by N^2 times:

$$A_s'(\omega_0) = \frac{A_N(\omega_0)}{N} = \frac{A_s(\omega_0)}{N^2}. \tag{12}$$

This suppression effect is in great contrast to the enhancement effect in the emission. It is caused by the N-fold enhanced coupling rate, which drives the resonator further away from the critical-coupling condition and leads to a weaker absorption. It is interesting to recognize that for a single weakly absorptive resonator alone, if we increase the coupling rate by N times, the absorption can only be reduced by N times, instead of N^2 times. Here the superradiant suppression of N^2 times is a coherent effect due to the far-field interaction among resonators.

Second, for strongly absorptive resonators $\gamma_0 \gg N\gamma_c$, above coherent effect is quenched. In this regime, a single resonator's absorption is $A_s \approx 4\gamma_c/\gamma_0$ when it is alone. For N resonators, Eq. (10) gives us a total absorption $A_N = NA_s$, a simple incoherent summation of N resonators. Individual resonators in the N-resonator system have the same absorption as the case when they are alone. In other words, the absorption of resonator is not affected by the presence of others.

Lastly, Eq. (10) also shows a superradiance-induced transparency effect: When $N \to \infty$, the total absorption approaches zero independent of the values of γ_0 and γ_c [Fig. 1(e)].

To demonstrate the above superradiant absorption effects, we perform simulations by numerically solving the full-wave Maxwell's equations. The nanoresonator is based on graphene ribbons. Graphene can be modeled using surface conductivity. Under random phase approximation, conductivity of graphene can be expressed in intraband and interband parts [29]. For the frequency range when $\hbar\omega \ll E_F$, the interband part can be neglected leaving only the intraband part as

$$\sigma_s^{intra} = \frac{2e^2 k_B T}{\pi\hbar^2}\ln\left(2\cosh\frac{E_F}{2k_B T}\right)\frac{i}{\omega + i\tau^{-1}}, \tag{13}$$

where E_F is chemical potential and τ is relaxation time. Thus, conductivity of graphene is expressed in Drude-like form. The effective permittivity of graphene used for numerical simulation is obtained as [30]

$$\varepsilon(\omega) = 1 + i\frac{\sigma_s}{\varepsilon_0\omega\Delta}, \tag{14}$$

where Δ is the thickness of graphene. This equation is in identical form to the Drude model equation where plasma frequency can be expressed as

$$\omega_p = \left[\frac{2e^2 k_B T}{\pi\hbar^2\varepsilon_0\Delta}\ln\left(2\cosh\frac{E_F}{2k_B T}\right)\right]^{1/2}. \tag{15}$$

In our simulation, $\Delta = 1$ nm, $E_F = 0.4$ eV, leading to plasma frequency $\omega_p = 2.3\times10^{15}$rad/s.

A 250-nm-wide ribbon has a fundamental resonant mode with a free-space wavelength around 20 μm [Fig. 1(a)].

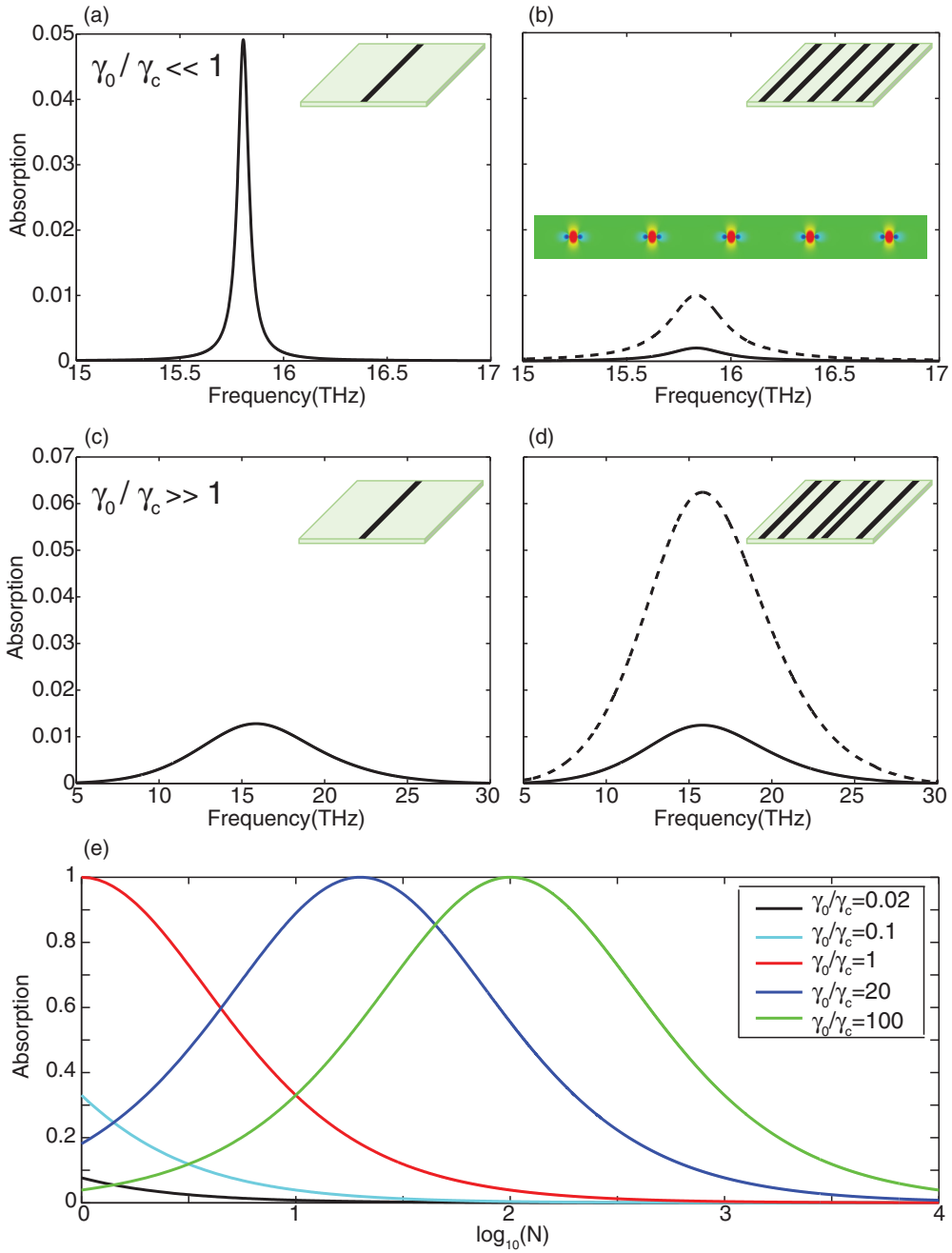

FIG. 1. (Color online) Superradiant absorption in graphene ribbon nanoresonators, for weakly [(a),(b)] and highly [(c),(d)] absorptive cases. (a) Absorption by a single ribbon with a low collision frequency 5×10^{9} s^{-1}. (b) The superradiance of five ribbons suppresses the total absorption by five times (dashed line). Individual ribbon's absorption (solid line) is suppressed by 25 times. Inset: the schematic of the structures (not to scale). Middle inset: the field distribution of the superradiant mode. (c) Absorption by a single ribbon with a high collision frequency 1.25×10^{14} s^{-1}. (d) The superradiance of five ribbons enhances the total absorption by five times (dashed line). Individual ribbon's absorption (solid line) remains the same. The substrate has a refractive index $n = 2$ and a thickness 2400 nm. Each ribbon is 250 nm wide, 1 nm thick, and infinitely long. The simulation domain is 10 μm wide. (e) The total absorption as a function of N calculated using Eq. (10). Independent of the ratio of the absorption γ_0 and coupling γ_c rates, transparency is induced by the superradiance with increasing N.

Since the electric fields are tightly confined to the edges of ribbons, the near-field interaction is minimal even when they are placed closely. These properties are difficult to achieve in conventional dielectric materials. In the simulations, a transverse magnetic plane wave is normally incident from the top. A large computational domain is used to ensure sufficient spacing between ribbons. The spacings between ribbons can be equal [Fig. 1(b)] or random [Fig. 1(d)] as long as near-field interactions remain minimal. The specific boundary conditions do not affect the physics. A periodic boundary condition is used while perfect reflecting boundary conditions would produce the same effects.

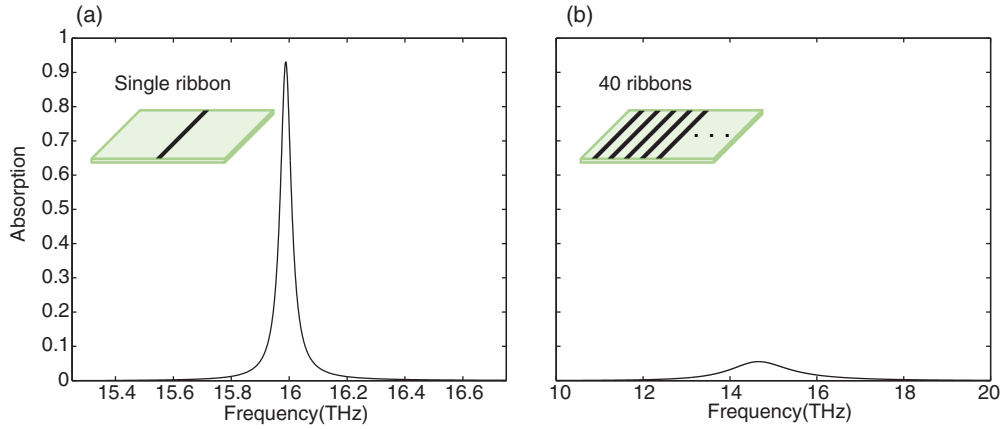

FIG. 2. (Color online) (a) Single ribbon having absorption close to 100%. (b) Superradiant-induced transparency using 40 identical ribbons. The computational domain is 18 μm with a periodic boundary condition. The collision frequency is $\gamma = 1.25\times10^{11}$ s^{-1} and the doping level is 0.4 eV. The ribbon width is 250 nm on 2.5 μm thick substrate ($n = 2$).

First, we study the weakly absorptive case when $\gamma_0/\gamma_c \ll 1$. The superradiance of five ribbons [Fig. 1(b) inset] suppresses the individual ribbons' absorption by 25 times [solid line, Fig. 1(b)] compared to when they are alone [Fig. 1(a)]. The total absorption of five ribbons [dashed line, Fig. 1(b)] is only 1/5 of the absorption of a single ribbon alone. For the strongly absorptive regime $\gamma_0/\gamma_c \gg 1$, we use a high collision frequency of graphene to increase the absorption rate γ_0. In this case, the superradiance barely affects the individual resonators' absorption [solid line, Fig. 1(d)] compared to that of a single ribbon alone [Fig. 1(c)]. The total absorption of five ribbons is enhanced by five times as a result of incoherent addition [dashed line, Fig. 1(d)].

When N is sufficiently large, the superradiance induces a transparency effect with the absorption approaching zero. Such transparency effect is independent of the ratio of γ_0 and γ_c [Fig. 1(e)]. The simulation of superradiance-induced transparency is shown in Fig. 2. When the absorption rate is close to the coupling rate, a single graphene resonator has a high absorption above 90% [Fig. 2(a)]. For 40 identical ribbons, the superradiance significantly increases the coupling rate. As a result, the absorption is reduced close to zero [Fig. 2(b)].

In the above discussion of the direct analog of quantum emitters, we have intentionally avoided the near-field interaction. In fact, near-field interactions when properly managed can also create superradiance. The near-field elements $\Omega_{ij}(i \neq j)$ in the Hamiltonian Ω hybridize N resonators to form a new set of eigenmodes $U\boldsymbol{a}$, where U is a unitary transformation that diagonalizes Ω. The new eigenmodes couple to the free-space radiation with a coupling strength UD^T. We next show that if all $\Omega_{ij}(i \neq j)$ have the same sign, the superradiance always occurs with all resonators oscillating in-phase. Moreover, this superradiant mode will either have the highest or the lowest eigenfrequency.

It is straightforward to show that Ω_{ij} $(i \neq j)$ can be expressed in real numbers if the system preserves the time-reversal symmetry. To see this, we write the resonators' fields in real functions, which is always possible for standing waves. Then, the time-reversal operator T has no effect on the fields, which means that the Hamiltonian matrix satisfies $T\Omega = \Omega T$. Therefore Ω must be real. Here we have neglected the absorption without affecting the conclusion. In addition, energy conservation requires $\Omega_{ij} = \Omega^*_{ji}$ [27], which leads to $\Omega_{ij} = \Omega_{ji}$.

Next, we show that if $\Omega_{ij}(i \neq j) > 0$, the superradiant mode always exists at highest eigenfrequency. For the normalized eigenmode with the highest frequency, we can write it as $|s\rangle = \sum_{i=1,K} c_i|a_i\rangle - \sum_{1=K+1,N} c_i|a_i\rangle$ with positive and real c_i when the system preserves the time-reversal symmetry. Now we define another state $|x\rangle = \sum_{i=1,K} c_i|a_i\rangle + \sum_{i=K+1,N} c_i|a_i\rangle$, and evaluate

$$\rho \equiv \langle s|\Omega|s\rangle - \langle x|\Omega|x\rangle = -4\sum_{i=K+1}^{N}\sum_{j}^{K} c_i c_j \Omega_{ij} \qquad (16)$$

Since $|s\rangle$ is the eigenmode with the highest frequency, the variational theorem requires $\rho \geqslant 0$. However, the coefficients on the right-hand side of Eq. (16) determine that ρ must be nonpositive. Therefore $\rho = 0$ and $N = K$, i.e., all N resonators are oscillating with the same phase. Similarly, we can show that if near-field interactions are all negative $\Omega_{ij} < 0$, the superradiance mode always exists and is located at the lowest eigenfrequency.

For numerical simulations, we configure the spatial arrangement of graphene ribbons to tune their near-field interactions. Figure 3(a) shows the distribution of the electric field around a graphene ribbon resonator. The near-field interaction is determined by the field overlap $\int_{V_j} E_i(\vec{r})E_j(\vec{r})[1-\varepsilon(\vec{r})]d\vec{r}$, where E_i and E_j are the electric fields generated by the ith [red lines, Figs. 3(b) and 3(c)] and jth [blue lines, Figs. 3(b) and 3(c)] resonators, respectively. The integration is performed on the site of the jth resonator V_j. The dielectric constant of graphene is negative. For a side-by-side configuration [Fig. 3(b)], the opposite directions of the fields lead to $\Omega_{ij} < 0$. For a top-bottom configuration, the aligned fields lead to $\Omega_{ij} > 0$.

To highlight the near-field effect in the simulation, we detune the resonant frequencies of N ribbons. The detuning suppresses the far-field interaction. But the near-field interactions are made strong enough to survive the detuning and become the main mechanism responsible for the superradiance. For five ribbons in a side-by-side configuration, all $\Omega_{ij} < 0$. The

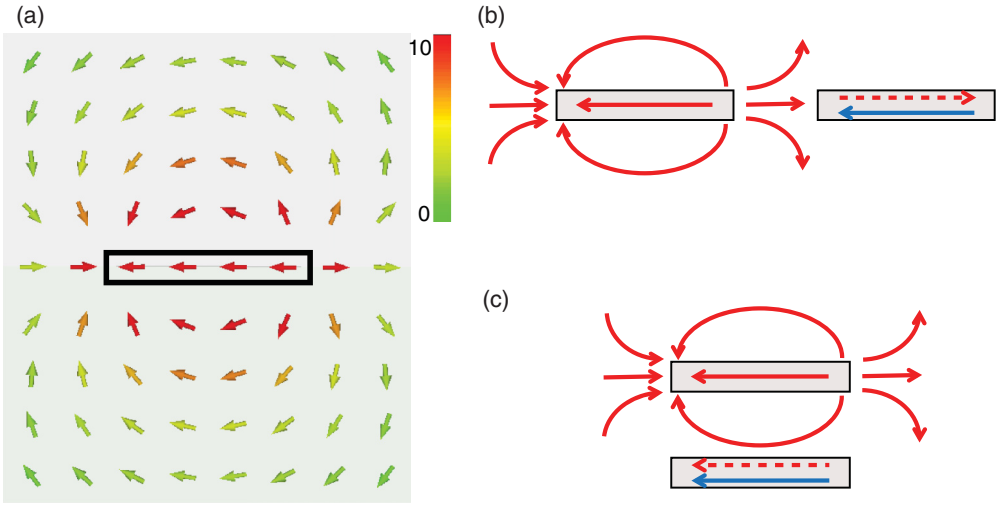

FIG. 3. (Color online) Near-field interactions among nearby graphene ribbons. (a) The electric field distribution of a ribbon resonator. (b) Negative interaction in the side-by-side configuration. The field generated by resonator i (red dashed arrow) is in the opposite direction of that of resonator j (blue arrow). (c) Positive interaction in the top-bottom configuration where fields are in the same direction.

superradiant mode creates a broad absorption peak [Fig. 4(b)] at the lowest frequency with all resonators oscillating in-phase [Fig. 4(a)]. It also has a much broader bandwidth compared to those of individual resonators alone [red lines, Fig. 4(b)]. The bandwidth broadening is a direct consequence of the enhanced superradiant coupling.

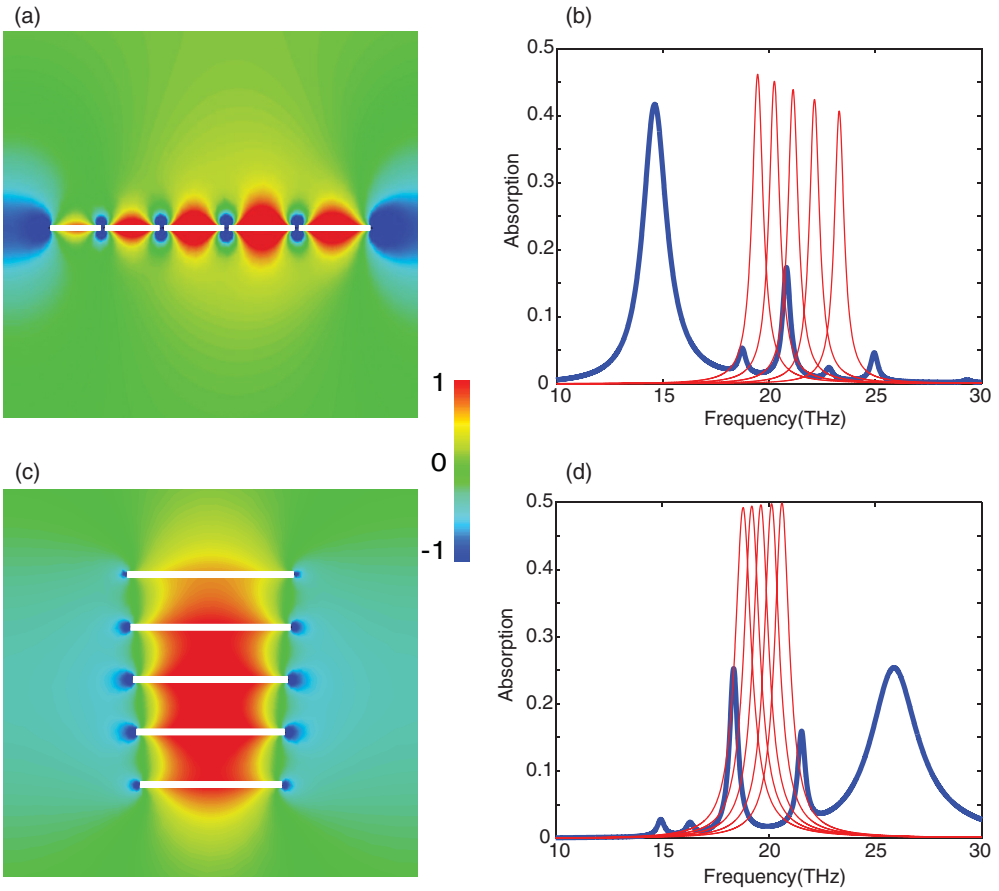

FIG. 4. (Color online) Near-field superradiance. (a) The electric field distribution of the superradiant mode in the side-by-side configuration. Ribbons (white bars) are spaced by 10 nm. Their widths are 280, 310, 340, 370, and 400 nm from the left to the right. (b) The superradiant mode has the lowest frequency (blue line). (c) The superradiant mode of five ribbons with widths 400, 385, 370, 355, and 340 nm from the top to the bottom. The spacing is 130 nm. (d) The superradiant mode has the highest frequency (blue line). The size of simulation domains for (a) and (c) are 2.24 and 1.5 μm, respectively. The collision frequency is 2.5×10^{12} s^{-1}. Red lines in (b) and (d) are the absorption spectra of individual ribbons when they are alone.

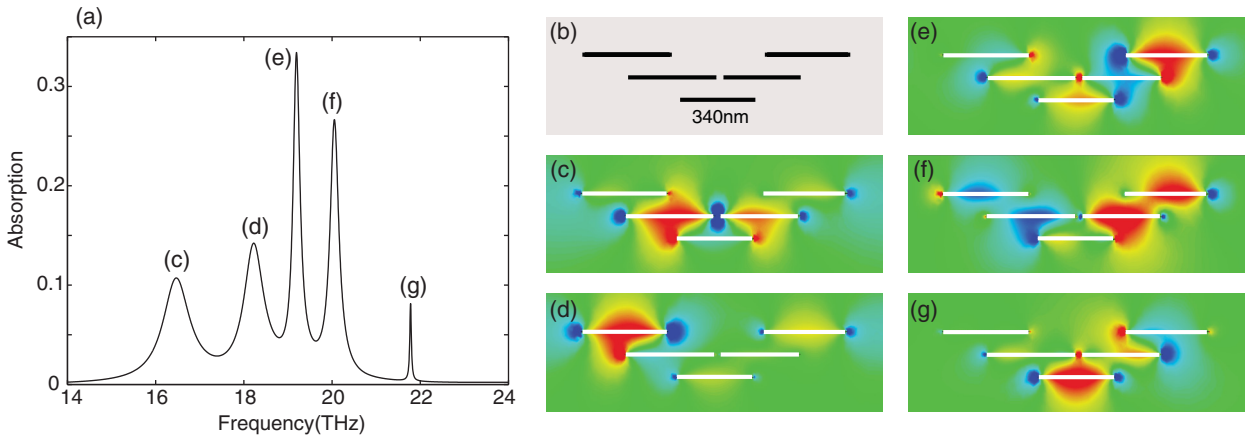

FIG. 5. (Color online) (a) Absence of superradiant mode in five ribbons arranged with mixed positive and negative near-field interactions. (b) The schematic of the structure. (c)–(f) The electric field distributions of resonances, showing no in-phase oscillation. The collision frequency is 2.5×10^{11} s^{-1}.

In contrast, for five ribbons in a top-bottom configuration [Fig. 4(c)], all $\Omega_{ij} > 0$. The superradiant mode [Fig. 4(c)] creates a broad absorption peak at the highest frequency [Fig. 4(d)], again featuring broadened bandwidth. When the near-field interactions are not properly managed with mixed signs such as the case shown in Fig. 5(b), there is no superradiant mode [Fig. 5(a)]. None of the resonant modes [Figs. 5(c)–5(g)] shows the in-phase oscillation.

Similar to the far-field case, the near-field superradiance has the same effect on light absorption. Unlike the far-field superradiance, the coupling rate typically increases by less than N times. To show this, we first note that the total coupling rates of all resonators are conserved despite the hybridization of resonators due to near-field interactions. Without near-field interactions, the total coupling rates to each channel are given by the diagonal elements of the matrix DD^T. With near-field interactions, the new coupling rates of the hybridized eigenstates are $D' = DU^{-1}$. The total coupling rates remain the same, $D'D'^T = DD^T$. The near-field interaction only redistributes coupling rates among resonances. The superradiant mode has to enhance its coupling at the expense of decreased coupling for other modes. In the far-field case, the superradiant mode is the only mode coupling to the free space and thus takes the entire coupling rate, leading to an N-fold enhancement. For the near-field case, other modes are typically not completely dark and the coupling rate of the superradiant mode normally does not increase by N times.

As a final remark, we discuss potential applications of superradiance in solar cells and photodetectors. Most subwavelength nanoresonators have very weak coupling to the free space because of their extremely small sizes. The imbalance of the absorption and the coupling rates leads to overall weak absorption, which limits the performance of the conversion from photons to charge carriers. The enhanced coupling rate in superradiance could allow nanoresonators to operate closer to the critical-coupling condition, where the absorption and coupling rates are balanced. For example, graphene is a highly absorptive material. But one still needs to rely on optical resonances in order to achieve 100% absorption in a single layer. For this purpose, the coupling rate of graphene resonators needs to be greatly enhanced to match the strong absorption rate. A recent proposal [20] showed the enhancement of coupling through careful choices of materials, such as a low-index substrate ($n = 1.45$) and a high doping level 0.4 eV. These choices turn out to be experimentally difficult, particularly for the midinfrared spectral range where low-index transparent materials are rare. Alternatively, we could use superradiance to enhance the coupling rate. The material requirement can be relaxed. For instance, Fig. 6 shows the perfect absorption with the superradiance of four graphene ribbons doped only at 0.2 eV on a high-index Si substrate making it much easier to achieve in experiment because of easy fabrication and excellent infrared transparency in Si.

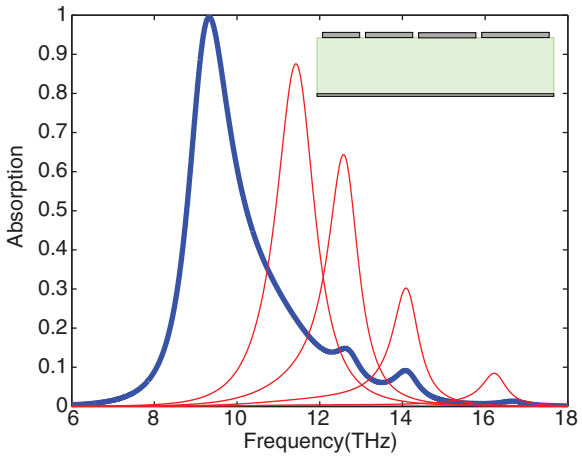

FIG. 6. (Color online) Perfect absorption achieved by the superradiance of four graphene ribbons. The graphene ribbons are doped at a low level of 0.2 eV and sit on a 2-μm-thick Si ($n = 3.42$) substrate. The widths of ribbons are 45, 60, 75, and 90 nm with 5 nm spacing. The periodicity is 315 nm. The substrate is on a reflecting mirror. $\omega_p = 1.62\times10^{15}$ rad/s, and collision frequency $\gamma = 4.5\times10^{12}$ s^{-1}. The superradiance creates an absorption peak with 100% absorption. Moreover, the peak has enhanced bandwidth compared to individual ribbons alone (red lines, Fig. 6).

[1] R. H. Dicke, Phys. Rev. **93**, 99 (1954).
[2] S. Zhang, D. A. Genov, Y. Wang, M. Liu, and X. Zhang, Phys. Rev. Lett. **101**, 047401 (2008).
[3] B. Luk'yanchuk, N. I. Zheludev, S. A. Maier, N. J. Halas, P. Nordlander, H. Giessen, and C. T. Chong, Nat. Mater. **9**, 707 (2010).
[4] Q. Xu, S. Sandhu, M. L. Povinelli, J. Shakya, S. Fan, and M. Lipson, Phys. Rev. Lett. **96**, 123901 (2006).
[5] M. F. Yanik, W. Suh, Z. Wang, and S. Fan, Phys. Rev. Lett. **93**, 233903 (2004).
[6] L. Maleki, A B. Matsko, A. A. Savchenkov, and V. S. Ilchenko, Opt. Lett. **29**, 626 (2004).
[7] D. D. Smith, H. Chang, K. A. Fuller, A. T. Rosenberger, and R. W. Boyd, Phys. Rev. A **69**, 063804 (2004).
[8] M. Fleischhauer and J. P. Marangos, Rev. Mod. Phys. **77**, 633 (2005).
[9] A. E. Miroshnichenko, S. Flach, and Y. S. Kivshar, Rev. Mod. Phys. **82**, 2257 (2010).
[10] Q. Xu, P. Dong, and M. Lipson, Nat. Phys. **3**, 406 (2007).
[11] C. Wu, A. B. Khanikaev, R. Adato, N. Arju, A. A. Yanik, H. Altug, and G. Shvets, Nat. Mater. **11**, 69 (2012).
[12] K. J. Boller, A. Imamoglu, and S. E. Harris, Phys. Rev. Lett. **66**, 2593 (1991).
[13] U. Fano, Phys. Rev. **124**, 1866 (1961).
[14] J. Pan, S. Sandhu, Y. Huo, N. Stuhrmann, M. L. Povinelli, J. S. Harris, M. M. Fejer, and S. Fan, Phys. Rev. B **81**, 041101 (2010).
[15] P. Lalanne and J. P. Hugonin, Nat. Phys. **2**, 551 (2006).
[16] N. E. Rehler and J. H. Eberly, Phys. Rev. A **3**, 1735 (1971).
[17] L. Ju, B. Geng, J. Horng, C. Girit, M. Martin, Z. Hao, H. A. Bechtel, X. Liang, A. Zettl, Y. R. Shen, and F. Wang, Nat. Nanotechnol. **6**, 630 (2011).
[18] M. Jablan, H. Buljan, and M. Soljačić, Phys. Rev. B **80**, 245435 (2009).
[19] H. Yan, X. Li, B. Chandra, G. Tulevski, Y. Wu, M. Freitag, W. Zhu, P. Avouris, and F. Xia, Nat. Nanotechnol. **7**, 330 (2012).
[20] S. Thongrattanasiri, F. H. L. Koppens, and F. J. García de Abajo, Phys. Rev. Lett. **108**, 047401 (2012).
[21] L. Verslegers, Z. Yu, Z. Ruan, P. B. Catrysse, and S. Fan, Phys. Rev. Lett. **108**, 083902 (2012).
[22] Y. Sonnefraud, N. Verellen, H. Sobhani, G. A. E. Vandenbosch, V. V. Moshchalkov, P. V. Dorpe, P. Nordlander, and S. A. Maier, ACS Nano **4**, 1664 (2010).
[23] P. A. Huidobro, A. Y. Nikitin, C. González-Ballestero, L. Martín-Moreno, and F. J. García-Vidal, Phys. Rev. B **85**, 155438 (2012).
[24] Z. Yu, A. Raman, and S. Fan, Proc. Natl. Acad. Sci. U.S.A. **107**, 17491 (2010).
[25] Z. Yu, A. Raman, and S. Fan, Phys. Rev. Lett. **109**, 173901 (2012).
[26] D. F. Walls and G. J. Milburn, *Quantum Optics* (Springer-Verlag, Berlin, 1995), p. 121.
[27] H. A. Haus, *Waves and Fields in Optoelectronics* (Prentice-Hall, Englewood Cliffs, NJ, 1984), p. 212.
[28] W. Suh, Z. Wang, and S. Fan, IEEE J. Quantum Electron. **40**, 1511 (2004).
[29] G. W. Hanson, J. Appl. Phys. **103**, 064302 (2008).
[30] A. Vakil and N. Engheta, Science **332**, 1291 (2011).